

Blazars in the LOFAR Two-Metre Sky Survey First Data Release

S. Mooney^{1,★}, J. Quinn¹, J. R. Callingham², R. Morganti^{2,3}, K. Duncan⁴, L. K. Morabito⁵, P. N. Best⁶, G. Gürkan⁷, M. J. Hardcastle⁸, I. Prandoni⁹, H. J. A. Röttgering⁴, J. Sabater⁶, T. W. Shimwell², A. Shulevski¹⁰, C. Tasse^{11,12}, and W. L. Williams⁸

¹ School of Physics, University College Dublin, Belfield, Dublin 4, Republic of Ireland

² ASTRON, Netherlands Institute for Radio Astronomy, PostBus 2, 7990 AA, Dwingeloo, The Netherlands

³ Kapteyn Astronomical Institute, University of Groningen, P.O. Box 800, 9700 AV Groningen, The Netherlands

⁴ Leiden Observatory, Leiden University, P.O. Box 9513, NL-2300 RA Leiden, the Netherlands

⁵ Astrophysics, University of Oxford, Denys Wilkinson Building, Keble Road, Oxford OX1 3RH, UK

⁶ SUPA, Institute for Astronomy, Royal Observatory, Blackford Hill, Edinburgh, EH9 3HJ, UK

⁷ CSIRO Astronomy and Space Science, PO Box 1130, Bentley WA 6102, Australia

⁸ Centre for Astrophysics Research, School of Physics, Astronomy and Mathematics, University of Hertfordshire, College Lane, Hatfield AL10 9AB, UK

⁹ INAF - Istituto di Radioastronomia, Via P. Gobetti 101, 40129 Bologna, Italy

¹⁰ Anton Pannekoek Institute for Astronomy, University of Amsterdam, Postbus 94249, 1090 GE Amsterdam, The Netherlands

¹¹ GEPI & USN, Observatoire de Paris, Université PSL, CNRS, 5 Place Jules Janssen, 92190 Meudon, France

¹² Department of Physics & Electronics, Rhodes University, PO Box 94, Grahamstown, 6140, South Africa

Received 24 July 2018; accepted 18 October 2018

ABSTRACT

Historically, the blazar population has been poorly understood at low frequencies because survey sensitivity and angular resolution limitations have made it difficult to identify megahertz counterparts. We used the LOFAR Two-Metre Sky Survey (LoTSS) first data release value-added catalogue (LDR1) to study blazars in the low-frequency regime with unprecedented sensitivity and resolution. We identified radio counterparts to all 98 known sources from the Third *Fermi*-LAT Point Source Catalogue (3FGL) or Roma-BZCAT Multi-frequency Catalogue of Blazars (5th edition) that fall within the LDR1 footprint. Only the 3FGL unidentified γ -ray sources (UGS) could not be firmly associated with an LDR1 source; this was due to source confusion. We examined the redshift and radio luminosity distributions of our sample, finding flat-spectrum radio quasars (FSRQs) to be more distant and more luminous than BL Lacertae objects (BL Lacs) on average. Blazars are known to have flat spectra in the gigahertz regime but we found this to extend down to 144 MHz, where the radio spectral index, α , of our sample is -0.17 ± 0.14 . For BL Lacs, $\alpha = -0.13 \pm 0.16$ and for FSRQs, $\alpha = -0.15 \pm 0.17$. We also investigated the radio-to- γ -ray connection for the 30 γ -ray-detected sources in our sample. We find Pearson's correlation coefficient is 0.45 ($p = 0.069$). This tentative correlation and the flatness of the spectral index suggest that the beamed core emission contributes to the low-frequency flux density. We compare our sample distribution with that of the full LDR1 on colour-colour diagrams, and we use this information to identify possible radio counterparts to two of the four UGS within the LDR1 field. We will refine our results as LoTSS continues.

Key words. surveys – radiation mechanisms: non-thermal – radio continuum: galaxies – gamma rays: galaxies – galaxies: active – (galaxies:) BL Lacertae objects: general

1. Introduction

The centres of some galaxies are extremely luminous, producing broadband non-thermal emission. These compact regions are known as active galactic nuclei (AGN). Some fraction of AGN are understood to have relativistic jets and by chance some of the jets are orientated close to our line of sight. Such AGN are known as blazars (see the review by Urry & Padovani 1995). The jets are believed to be powered by the accretion of matter onto supermassive black holes residing at the galactic cores. Relativistic beaming effects give rise to apparent superluminal motion, and Doppler boosting increases the observed luminosity. Although blazars are the most common sources in the γ -ray regime (Acero et al. 2015), only a small number of blazars are γ -ray-loud and the reasons for this are still unclear (Fan et al. 2012).

There are two types of blazars that are distinguished by their observational properties: BL Lacertae objects (BL Lacs) and flat-spectrum radio quasars (FSRQs). The populations are defined by the presence or absence of strong emission lines, which is controlled by the inner accretion disc. BL Lacs possess featureless optical spectra and are generally associated with beamed jet-mode (radiatively inefficient) AGN. In contrast, strong optical emission lines are a characteristic of FSRQs and they are often associated with beamed radiative-mode AGN. However, one commonality shared by BL Lacs and FSRQs is the broadband nature of the radiation they emit.

The characteristic structure seen in the spectral energy distributions (SEDs) for blazars consists of two components in the $\nu F_\nu - \nu$ plane (where ν is frequency and F_ν is flux), which has the non-thermal components dominating energetically over the thermal component at all wavelengths. These two components give the blazar SEDs their characteristic double-humped shape.

* sean.mooney@ucdconnect.ie

The first component begins in the radio waveband and peaks in the optical or X-ray waveband. This emission can be attributed to synchrotron processes from a population of relativistic (\gtrsim keV) electrons in a magnetic field. Blazars typically possess flat spectra at gigahertz frequencies, where the radio spectral index, α , is defined as $S(\nu) \propto \nu^\alpha$, typically $\alpha > -0.5$. Nori et al. (2014) found that blazars have flat spectra down to ~ 300 MHz. At lower frequencies, the spectrum becomes inverted (i.e. $\alpha > 0$) because of synchrotron self-absorption.

The second feature of the SED peaks between the MeV and TeV energy bands and may be caused by inverse-Compton scattering (e.g. Sikora et al. 1994) but this remains an open question (Beckmann & Shrader 2012). If this is the case, then seed photons originating from the synchrotron process are inverse-Compton scattered by the electrons in the jet to higher energies (i.e. synchrotron self-Compton radiation; Marscher & Gear 1985). However, it is also possible that the seed photons originate from outside the jet – for example, from the accretion disc or broad line region. Alternatively, the high-energy peak of the SED may be the result of hadronic synchrotron processes, rather than leptonic inverse-Compton processes (Böttcher 2007).

We search for a correlation between the low-frequency radio emission and the γ -ray emission in this study. The existence of such a correlation is still debated (Pavlidou et al. 2012). Several studies have found a correlation (Stecker et al. 1993; Padovani et al. 1993; Salamon & Stecker 1994; Ackermann et al. 2011; Linford et al. 2012). However, taking all biases into account, such as the limited dynamic range (when considering flux densities) or the common redshift dependence (when considering luminosities) is non-trivial (Kovalev et al. 2009). For example, Mücke et al. (1997) and Chiang & Mukherjee (1998) disputed evidence of a correlation on the grounds of redshift biases and the sensitivity limits of the surveys used.

Studying blazars at megahertz frequencies is challenging because their characteristic flat spectra make it difficult to identify counterparts in this regime. For example, Giroletti et al. (2016) used the Murchison Widefield Array Commissioning Survey (MWACS) (Hurley-Walker et al. 2014) to examine the 120–180 MHz emission from blazars. The MWACS has $\sim 3'$ angular resolution and a typical noise level of 40 mJy beam^{-1} , which allowed Giroletti et al. (2016) to identify low-frequency counterparts to 186 of 517 (36%) blazars in the MWACS footprint. Giroletti et al. (2016) then calculated the mean low-frequency spectral index to be -0.57 ± 0.02 , and identified a mild correlation between the radio flux density and the γ -ray energy flux ($r = 0.29$, $p = 0.061$). Callingham et al. (2017) also identified a small number of blazars that show a peaked spectrum in the low-frequency spectra from the GLEAM survey (Hurley-Walker et al. 2017). This emphasises that a simple selection of flat-spectrum radio sources may not select all blazars. However, both Callingham et al. (2017) and Giroletti et al. (2016) were limited in their resolution and sensitivity to explore the population in depth.

We use the LOFAR Two-Metre Sky Survey (LoTSS) first data release value-added catalogue (LDR1) to study the 144 MHz properties of blazars (Shimwell et al. in press; Williams et al. submitted; Duncan et al. in press). We cross-matched LDR1 with the Third *Fermi*-LAT Point Source Catalogue (3FGL) (Acero et al. 2015), the Roma-BZCAT Multi-frequency Catalogue of Blazars (5th edition) (Massaro et al. 2015), and the very-high-energy catalogue called TeVCAT (Wakely & Horan 2008). The LDR1 catalogue covers 424 deg^2 of the sky with future data releases aiming to significantly expand this to full coverage of the northern sky. In this respect, this work paves the way for a larger study with future data releases.

This paper is organised as follows: The sample of sources used for this study was constructed from several surveys and catalogues, each of which is described in turn in §2. The way in which we built our sample is detailed in §3. Our results are presented in §4 and discussed in §5. We use a Λ CDM cosmological model throughout this paper with $h = 0.71$, $\Omega_m = 0.26$, and $\Omega_\Lambda = 0.74$, where $H_0 = 100h\text{ km s}^{-1}\text{ Mpc}^{-1}$ is the Hubble constant. We maintain the definition of α , where $S(\nu) \propto \nu^\alpha$.

2. Surveys and catalogues

2.1. LOFAR Two-Metre Sky Survey First Data Release

The Low Frequency ARray (LOFAR) is a radio interferometer with stations located throughout Europe (van Haarlem et al. 2013). The LOFAR Surveys key science project aims to map the sky above the northern hemisphere between 120 MHz and 168 MHz. A full description of the LoTSS can be found in Shimwell et al. (2017). The LoTSS is underway, making use of the core and remote LOFAR stations in the Netherlands.

The first data release is outlined in Shimwell et al. (in press) and the value-added catalogue is outlined in Williams et al. (submitted) and Duncan et al. (in press). The LDR1 uses data collected between 2014 May 23 and 2015 October 15, focussing on the HETDEX Spring Field (Hill et al. 2008). The right ascension ranges approximately from 10 h 45 m 00 s to 15 h 30 m 00 s and the declination ranges approximately from $45^\circ 00' 00''$ to $57^\circ 00' 00''$; the advantage of this region for the study of blazars is that it is far from the galactic centre. Furthermore, the $6''$ angular resolution and $71\text{ }\mu\text{Jy beam}^{-1}$ median sensitivity of LDR1 is unrivaled with respect to existing radio surveys. To study the blazar population, we use this catalogue described in Shimwell et al. (in press), which has the direction-dependent corrections applied.

2.2. 3FGL and 3LAC

The 3FGL is based on data from the first four years of *Fermi*-LAT, covering the 0.1–300 GeV energy range (Acero et al. 2015). There are 3 033 sources in 3FGL, of which 1 009 are unassociated γ -ray sources (UGS). These are sources to which a known source could not be unambiguously linked, often due to source confusion.

The Third Catalogue of AGN detected by *Fermi*-LAT (3LAC) is the most comprehensive catalogue of γ -ray AGN at present. The 3LAC is based on 3FGL sources that have a test statistic > 25 (i.e. $\gtrsim 5\sigma$ significance) between 100 MeV and 300 GeV over the period extending from 2008 August 04 to 2012 July 31 (Ackermann et al. 2015). The 3LAC contains 1 773 AGN in total with 491 (28%) FSRQs, 662 (37%) BL Lacs, 585 (33%) blazars of unknown type, and 35 (2%) sources of other types. We use the improved source positions and blazar classification information in 3LAC to aid in the study of our sample.

2.3. BZCAT

BZCAT is a catalogue of blazars that contains multi-frequency data from a number of surveys (Massaro et al. 2015). The BZCAT contains radio flux measurements which are either at 1.4 GHz from the National Radio Astronomy Observatory Very Large Array Sky Survey (NVSS) (Condon et al. 1998) ($0.45\text{ mJy beam}^{-1}$ sensitivity) or at 0.8 GHz from the Sydney University Molonglo Sky Survey (SUMSS). For the region of sky we are interested in, the radio flux measurements used are

Table 1: Breakdown of our sample is shown according to catalogue and source type. The 3FGL includes 3LAC; the sole difference between these catalogues over the LDR1 footprint is the four UGS that are included in 3FGL only.

Catalogue	FSRQ	BL Lac	Uncertain type	BL Lac candidate	Blazar candidate	Galaxy dominated	Radio galaxy	UGS	Total
BZCAT only	41	12	4	1	0	10	0	0	68
3FGL only	0	0	0	0	3	0	1	4	8
BZCAT and 3FGL	8	15	3	0	0	0	0	0	26
Total	49	27	7	1	3	10	1	4	102

those at 1.4 GHz because sources in LDR1 have a declination $> -30^\circ$. The source positions are mostly derived from very-long-baseline interferometry measurements. In addition, BZCAT reports information from the Wide-field Infrared Survey Explorer (*WISE*) and the Sloan Digital Sky Survey (SDSS) optical database.

Edition 5.0.0 of BZCAT was used and, while 3FGL contains a higher fraction of BL Lacs, BZCAT lists mostly FSRQs. Of the 3 561 sources in BZCAT, 1 909 (54%) are FSRQs, 1 425 (40%) are BL Lacs, 227 (6%) are blazars of uncertain type, and 274 (8%) are galaxy-dominated blazars.

2.4. TeVCAT

We searched for sources in TeVCAT (Wakely & Horan 2008), which provides TeV data, but found no sources within the LDR1 footprint. However, this will become an important source of information with which to study blazars as LoTSS progresses.

3. Analysis

3.1. Sample construction

For the high-energy sources, BZCAT positional data were used where available, and 3LAC data were used secondarily. Both have accurately defined positions. Likewise, the source classifications (FSRQs, BL Lacs, etc.) were taken from BZCAT in the first instance and from 3LAC for sources without a BZCAT association. For the UGS, 3FGL positions were used, which had comparatively large uncertainty ellipses.

Using TOPCAT (Tool for Operations on Catalogues and Tables; Taylor 2005), we cross-matched the catalogues with LDR1, where the LDR1 positions take account of any extended features, not just the core regions. We implemented a 12'' search radius. Although this is comparatively large compared to the astrometric uncertainties (the average uncertainty on the position of an LDR1 source is $\sim 0.3''$), 93% of LDR1 sources were unique matches within 7'' of the BZCAT or 3LAC positions. The seven sources with a separation of 7–12'' are extended in LDR1, and also had unique matches within 12''. All matches were confirmed visually and images showing the sources in our sample along with the BZCAT/3LAC positions can be found at <https://github.com/mooneyseye/LDR1-blazars>.

An overview of the 102 unique extragalactic sources in our sample is given in Table 1, where 68 sources were in BZCAT only and therefore have no γ -ray detection. An LDR1 match was found for all sources, excluding the UGS; a unique match could not be determined for the four UGS because of source confusion.

To investigate the likelihood of spurious detections, we shifted all sources in BZCAT by 2° in a random direction and performed the same cross-matching procedure as before. We repeated this several times and found no matches within 7'' and ~ 2

Table 2: Number of sources found in each catalogue or survey. NVSS detected 97 of 98 BZCAT or 3FGL sources in the field. There are 8 sources detected in LDR1 and NVSS only.

Survey	ν (MHz)	BL Lacs	FSRQs	Other	Total
VLSSr	73.8	5	24	7	36
LDR1	144	27	49	22	98
TGSS	148	20	45	17	82
7C	151	10	37	13	60
WENSS	325	23	47	19	89
NVSS	1 400	26	49	22	97

matches within 10'', indicating that it is likely our sample is free from such spurious detections.

3.2. Radio spectral index

To calculate the radio spectral indices, flux density measurements from several surveys in the 0.07–1.4 GHz range were employed: the Very Large Array Low-frequency Sky Survey Redux (VLSSr) (Lane et al. 2014), the 7th Cambridge Survey of Radio Sources (7C), the Westerbork Northern Sky Survey (WENSS) (Rengelink et al. 1997), and NVSS were used where available. Table 2 shows the frequency corresponding to each survey and the number of sources for which each survey had data. The TIFR Giant Metrewave Radio Telescope Sky Survey First Alternative Data Release (TGSS ADR1) (Intema et al. 2017) was not used in spectral fitting but is shown in Table 2 to allow for comparisons.

The spectral modelling performed was identical to that done by Callingham et al. (2015). In summary, the Markov chain Monte Carlo (MCMC) algorithm emcee (Foreman-Mackey et al. 2013) was used to sample the posterior probability density functions of a power-law or a curved-power-law model (see equations 1 and 2 of Callingham et al. 2017). Physically sensible priors were applied (such as that the normalisation constant cannot be negative) and a Gaussian likelihood function was maximised by applying the simplex algorithm to direct the walkers (Nelder & Mead 1965). For this method, the uncertainties reported on the flux density values in all the surveys were assumed to be Gaussian and independent.

We compared the modelled spectral index to the spectral index where only the lowest (VLSSr where available, but LDR1 in the majority of cases) and highest frequencies (NVSS) were used, $\alpha_{\min-\max}$. We found $\alpha_{\min-\max} = -0.20 \pm 0.14$, and this is in agreement with $\alpha = -0.17 \pm 0.14$, when all points are used. The equation of the line between these quantities is $\alpha_{\min-\max} = 0.97\alpha - 0.03$, where $r = 0.96$, indicating that fitting a power law to the sources in our sample is a valid assumption.

Table 3: Summary of our results is shown. The flux density ($S_{144\text{ MHz}}$) and luminosity (L_ν) refer to median values; for the redshift (z) and spectral index (α) the average is given. The number of γ -ray-detected sources is N_γ .

Subsample	N	z	$S_{144\text{ MHz}}$ (mJy)	L_ν (W Hz)	α	N_γ
BL Lacs	27	0.776	69 ± 14	$(3.7 \pm 0.7) \times 10^{25}$	-0.13 ± 0.16	15
FSRQs	49	1.249	362 ± 72	$(1.4 \pm 0.3) \times 10^{27}$	-0.15 ± 0.16	8
Others	22	0.466	152 ± 30	$(5.8 \pm 1.2) \times 10^{25}$	-0.28 ± 0.19	7
Total	98	0.947	199 ± 40	$(2.7 \pm 0.5) \times 10^{26}$	-0.17 ± 0.14	30

The majority (83%) of our sources are found in both TGSS and NVSS and hence appear in the TGSS-to-NVSS spectral index catalogue (de Gasperin et al. 2018). These sources have an average TGSS-to-NVSS spectral index of -0.28 ± 0.15 , which is in keeping with our result of $\alpha = -0.24 \pm 0.14$ for the same sample.

3.3. Blazar variability

Blazars can exhibit flux variability from radio to γ -ray energies (Richards et al. 2011), making it necessary to assess the impact of any inherent variability on the derived spectral indices and the strength of the radio-to- γ -ray correlation.

The surveys used to calculate the spectral index are non-simultaneous, so it is possible that the flux densities used to fit α change over time. However, there is less radio variability in blazars below the synchrotron peak than above it (Urry 1998). In support of this, Bell et al. (2018) found that blazars do not seem to be significantly variable at low frequencies and McGilchrist & Riley (1990) found little variability of 7C sources at 151 MHz. Pandey-Pommier et al. (2016) monitored PKS 2155-304, one of the brightest BL Lacs, while it was flaring and found only marginal variability at 235 MHz. Furthermore, Turriziani et al. (2015) conducted a preliminary blazar monitoring programme with LOFAR at 226 MHz, focussing on five blazars which exhibit strong gigahertz variability. The LOFAR light curves revealed a smooth behaviour (with some possible changes to the flux of the order of months). Hence, it is the NVSS flux densities which we expect to be most affected by variability, since this was the only catalogue we used > 325 MHz. We included data from several megahertz surveys in the spectral modelling to minimise the influence of this possible variability, but the NVSS data are still the most influential when calculating α .

The LDR1 and 3FGL catalogues are non-contemporaneous: LDR1 observations were made between 2014 and 2015 while 3FGL observations were integrated between the years 2008 and 2012. As a result, for any blazars which exhibit strong γ -ray variability, the data in 3FGL correspond to an average value and are more indicative of the non-flaring state. Since we do not expect the 144 MHz or γ -ray data to be variable, we conclude that the non-simultaneity does not significantly impact any correlation between the radio and γ -ray bands.

4. Results

4.1. Detection rate and redshift

We identified LDR1 counterparts to 100% of the high-energy sources (excluding UGS) and a summary of our results are given in Table 3. Information on the individual 98 sources in our sample is presented in Table 6 at the end of this paper. In our sample, 48% of sources are FSRQs, 25% are BL Lacs, 8% are blazars of

uncertain type or BL Lac candidates, and 16% are other source types (e.g. galaxy-dominated blazars, AGN, radio galaxies, and UGS).

Most (77/98) redshifts are the spectroscopic LDR1 values. The remainder are from BZCAT (6/98), the NASA/IPAC Extragalactic Database (6/98), 3LAC (1/98), or are LDR1 photometric estimates (6/98); two sources have no measured redshift. Obtaining photometric redshifts for blazars is challenging owing to the lack of reliable SED templates, but the LDR1 photometric redshifts are dominated by machine learning estimates which do not depend on such templates. The caption of Table 6 contains a link to the CSV version of the table, which shows the origin of z for each source.

Fig. 1 shows the redshift distribution of our sample as well as the distributions of BZCAT and 3LAC. In BZCAT, 2 842 of the 3 561 sources have redshifts (see Fig. 1b), and in 3LAC, 896 of the 1 773 sources have a measured redshift (see Fig. 1c). The redshift distribution of our sample follows a similar trend to the BZCAT distribution, but in 3LAC there is a larger percentage of low-redshift BL Lacs. The FSRQ population is more distant than BL Lacs on average in all cases.

4.2. Flux density and luminosity

The 144 MHz radio flux density, $S_{144\text{ MHz}}$, in our sample ranges from 1.3 mJy to 14 Jy. The FSRQs have a higher median $S_{144\text{ MHz}}$ than the BL Lacs, as seen in Table 3. The median $S_{144\text{ MHz}}$ for γ -ray-detected sources (193 ± 105 mJy) and for non- γ -ray-detected sources (203 ± 19 mJy) are within error of each other.

We calculated the radio luminosity, L_ν (in W Hz $^{-1}$), according to

$$L_\nu = \frac{S_{144\text{ MHz}} 4\pi d^2}{(1+z)^{1+\alpha}},$$

where $S_{144\text{ MHz}}$ is in W m $^{-1}$ Hz $^{-2}$ and d is the luminosity distance in metres. Fig. 2 shows the distribution of L_ν for our sample. The FSRQs span a broad range of L_ν , while the BL Lacs are predominantly in the lower bins, as expected.

4.3. Radio spectral index

Fig. 3 shows the radio spectral index distribution, and the average values are given in Table 3. The average α for our sample is -0.17 ± 0.14 , and this is much flatter than α for all sources in LDR1, which we expect to be $-0.8 \lesssim \alpha \lesssim -0.7$. Our results suggest both BL Lacs and FSRQs are flat even at megahertz frequencies. We found $\alpha = -0.11 \pm 0.17$ for the γ -ray sources, which is similar to the non- γ -ray-detected blazars where $\alpha = -0.21 \pm 0.16$. Giroletti et al. (2016) found $\alpha = -0.57 \pm 0.02$, which is steeper than the α we calculated. This can be explained by the fact that all blazars in the field were detected in this study,

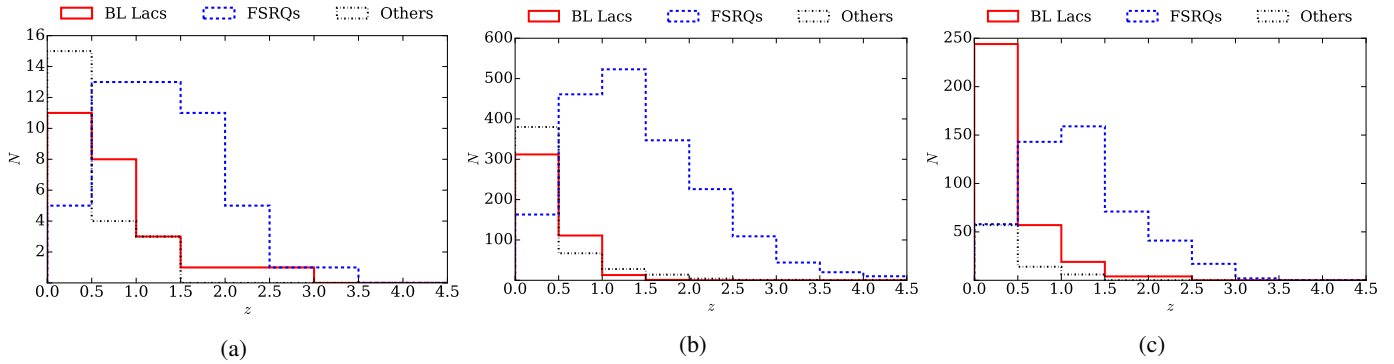


Fig. 1: Distribution of the measured redshift values in (a) our sample compared to (b) BZCAT and (c) 3LAC is shown. Included in “Others” are, for example, blazars of uncertain type, BL Lac candidates, and galaxy-dominated BL Lacs.

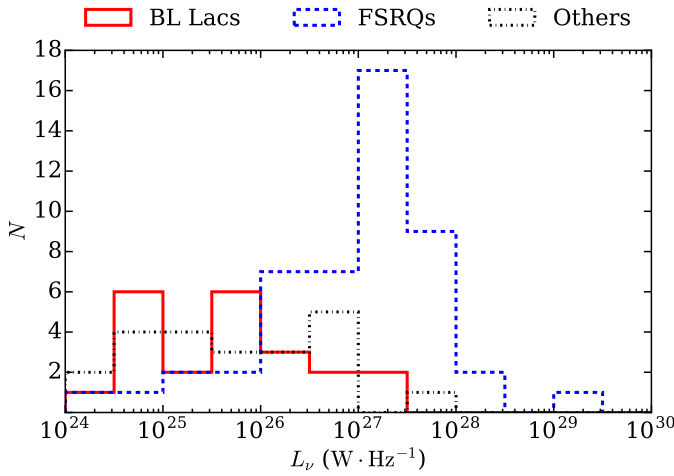


Fig. 2: Radio luminosity distribution for our sample is shown.

whereas Giroletti et al. detected 36% of blazars. This introduces a selection effect against flat or inverted-spectrum sources.

The contribution of the flat-spectrum core to the flux density is understood to decrease as the frequency decreases and, in the megahertz regime, the flux density is thought to be dominated by the extended emission in the radio lobes. However, the flatness of α suggests the beamed core emission is contributing somewhat to the low-frequency flux density. As our sample consists of blazars, Doppler boosting can lead to the core component appearing disproportionately brighter than the extended component.

The spectra for some sources in our sample appear to be gigahertz-peaked spectrum (GPS) sources (Callingham et al. 2017). An example is seen in Fig. 4, which shows the spectra from which α was derived for two sources in our sample. It has previously been argued that GPS quasars are flaring blazars (Tinti et al. 2005) or intrinsically young radio sources (Fanti et al. 1995).

4.4. Radio– γ -ray connection

Fig. 5 shows the radio flux density plotted against the γ -ray energy flux for the γ -ray-detected sources. The γ -ray energy flux at 100 MeV was calculated from the integrated photon flux given in 3FGL using the γ -ray power-law spectral index. Two sources not in the 3LAC “clean” sample and 3C 303 were excluded. A

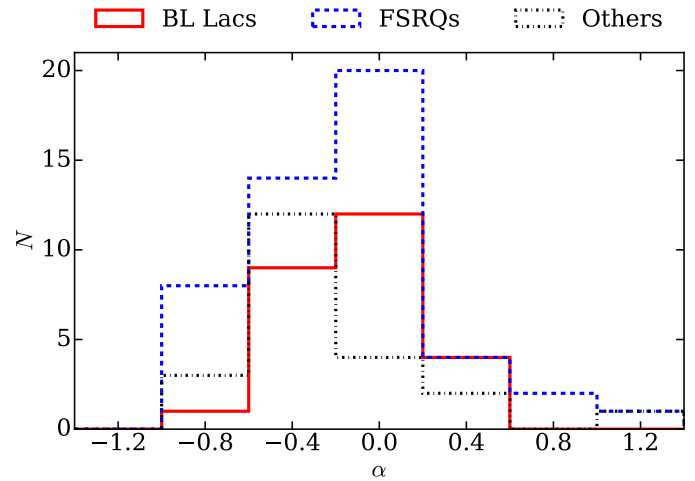


Fig. 3: Distribution of the radio spectral indices for the sources in our sample is shown.

linear fit to the logarithms of the flux yields a slope, and hence power-law index, of $m = 0.61 \pm 0.25$. We obtained a Pearson correlation coefficient, r , of 0.45 with a null-hypothesis p -value of 0.019. This marginally significant p -value is limited by our $N = 27$ sample size, and the sample sizes were too small to calculate the correlation with any meaningful significance for the BL Lac or FSRQ populations. This correlation also does not address the biases within the data.

We then used the Monte Carlo correlation method outlined by Pavlidou et al. (2012) in our radio-to- γ -ray analysis, which has also been used by Ackermann et al. (2011). This method was designed for small samples affected by distance effects and subjective sample selection criteria. The data are randomised in luminosity space. This accounts for the fact that the radio and γ -ray flux densities appear to be correlated because of their common redshift. Then the significance is measured in flux space to avoid Malmquist bias (Lister & Marscher 1997).

The Pavlidou et al. method gave the $r = 0.45$ correlation a significance of $p = 0.069$. This is therefore suggestive of a correlation, although we cannot conclusively reject the null hypothesis that the radio and γ -ray luminosities of blazars are independent. Furthermore, this method provides a conservative estimate for small samples and so, while real correlations may not be verified, exaggerated significances are avoided in cases where there is insufficient evidence.

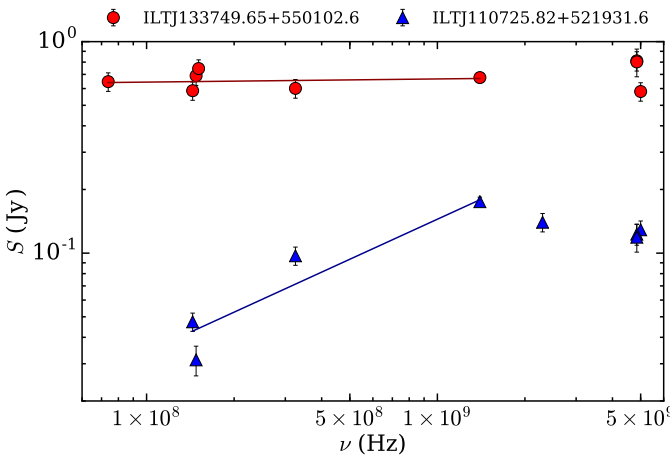


Fig. 4: Flat spectrum source and peaked spectrum source from our sample. The spectral fits we derived using data up to 1.4 GHz are shown as solid lines. Data from NED up to 5 GHz have been plotted. The flatness of the radio spectrum for ILTJ133749.65+550102.6 is clear, as is the GHz peak for ILTJ110725.82+521931.6.

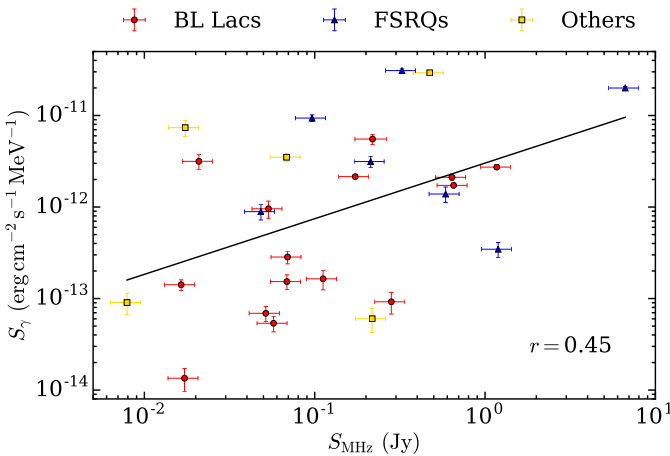


Fig. 5: γ -ray energy flux density is plotted against the radio flux density. A line was fit to the logarithms of the data. The radio flux density is at 144 MHz and the γ -ray energy flux density measurements correspond to 100 MeV.

This correlation is weaker than the gigahertz radio-to- γ -ray connection for the same sample ($r = 0.57$, $p = 0.002$), as we would expect, given that the emission is usually more diffuse at lower frequencies.

4.5. Colour-colour diagrams

In 2010, *WISE* observed the sky at $3.4\text{ }\mu\text{m}$ (W1), $4.6\text{ }\mu\text{m}$ (W2), $12\text{ }\mu\text{m}$ (W3), and $22\text{ }\mu\text{m}$ (W4). These magnitudes are included in LDR1, from which we calculated the colours. Fig. 6 shows the W1 – W2 – W3 colour-colour and colour-magnitude diagrams. Sources in our sample are plotted over the LDR1 catalogue, where LDR1 sources are predominantly star-forming galaxies. It is clear that blazars populate distinct regions compared to LDR1 on each of these plots, but the blazar population is the most compact in Fig 6a.

Table 4: List of UGS within the LDR1 footprint, along with the number of LDR1 sources within the 95% uncertainty ellipse. The 3FGL ellipse sizes vary considerably, leading to the large variation in the number of LDR1 matches. Also shown are the number of likely matches based on the colour information.

UGS name	LDR1 sources within 95%	Likely matches using colour data
3FGL J1051.0+5332	166	3
3FGL J1103.3+5239	82	1
3FGL J1231.6+4825	29	0
3FGL J1502.2+5553	5	0
Total	282	4

In Fig. 6a, the *WISE* blazar strip can be seen (Massaro et al. 2011). Generally, blazars are dominated by synchrotron emission in the infrared (IR) band. As a result, blazars have a distinct locus to that of the LDR1 sources, the majority of which are dominated by a thermal component in the IR. The distribution of blazars in Fig. 6a is in agreement with a power-law model for the IR spectrum. Moreover, BL Lacs and FSRQs also inhabit distinct regions on this colour-colour diagram, and the locations of these populations are consistent with the findings of Massaro et al. (2011). Some blazars lie outside the blazar strip, and in this case, it is possible that there is a non-negligible thermal contribution to the IR emission from the host galaxy.

Fig. 6b shows a different combination of IR colours, where the blazar population is also removed from the thermal LDR1 population. Fig. 6c plots the W1 magnitude, which is the band with the highest sensitivity, against the W1 – W2 colour. The blazars appear brighter than LDR1 sources of the same colour as a result of Doppler boosting. The majority of blazars have $W1 - W2 \approx 1$, as noted by D'Abrusco et al. (2012). This corresponds to an IR spectral index of -1 and suggests the synchrotron component peaks close to the *WISE* measurements. Furthermore, Stern et al. (2012) used $W1 - W2 > 0.8$ as criterion to select for AGN, as this distinguishes between the AGN power-law spectra and the galactic black-body spectra.

The four 3FGL UGS within the LDR1 footprint are shown in Table 4 alongside the number of LDR1 sources which fall within the 3FGL 95% ellipse. This is illustrated for 3FGL J1051.0+5332 in Fig. 7 where the semi-major and semi-minor axes are 0.213° and 0.155° , respectively. Colour information from *WISE* has previously been used to classify UGS by D'Abrusco et al. (2013). We also used the colour-colour diagrams to identify possible counterparts to the UGS on the basis that, statistically, these γ -ray sources are most likely to be blazars because blazars dominate the extragalactic γ -ray sky.

We chose 96 sources at random from LDR1 because colour information was available for 96 sources in our sample. We plotted these two populations on colour-colour diagrams (not shown) and used an inverse-distance-weighted k -nearest neighbours (k -NN) algorithm (where $k = 3$) to identify which UGS matches were likely to be blazars. From the total 282 possible LDR1 matches for the UGS, only four are likely to be blazars. Three matched with one source, one UGS had just a single possibility, and two UGS had no possible matches remaining. The properties of these potential matches are given in Table 5.

Advantages of this k -NN method are that it assumes no prior knowledge of the region inhabited by blazars in colour space and that the implementation is straightforward. Identifying two of four possible counterparts is a promising return and based on

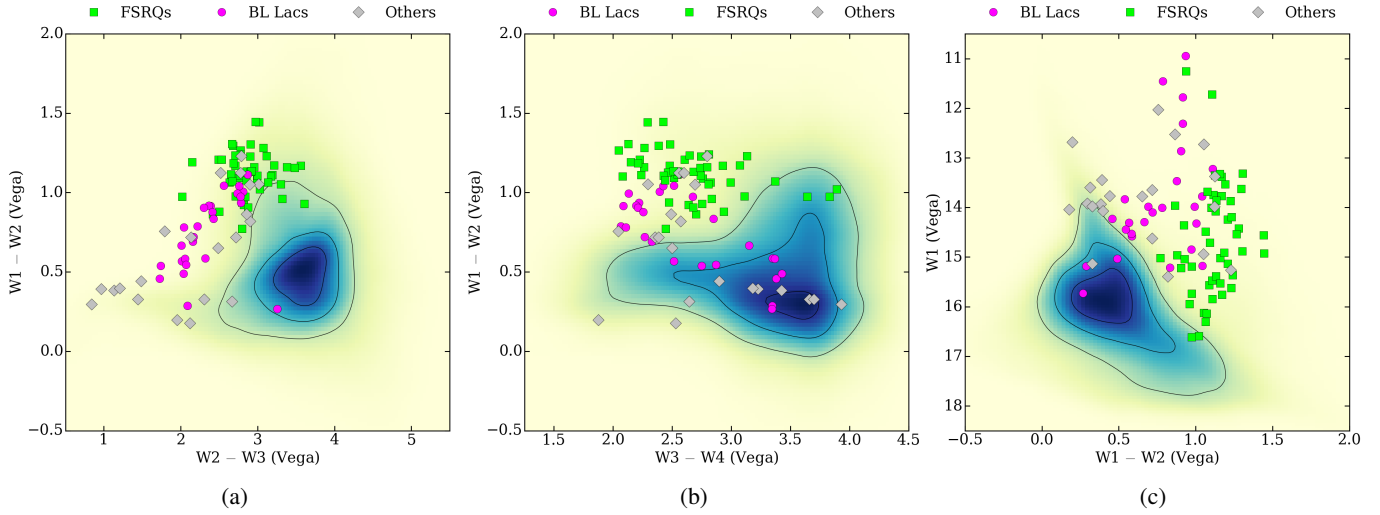


Fig. 6: Two-dimensional histograms show (a) the $W_1 - W_2$ vs. $W_2 - W_3$ and (b) the $W_1 - W_2$ vs. $W_3 - W_4$ colour-colour diagrams, and (c) the $W_1 - W_2$ vs. $W_1 - W_2$ colour-magnitude diagram. The IR colours for the entire LDR1 sample for which there is *WISE* data available (218 595 of 318 520 sources) is the two-dimensional histogram, with contours indicating the 25%, 50%, and 75% levels. The points are the LDR1 sources from our sample for which there is *WISE* data (96 of 98 sources).

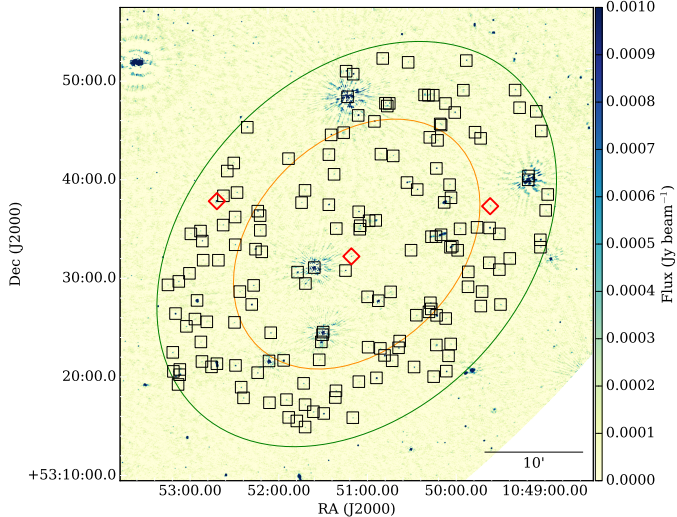


Fig. 7: Unassociated γ -ray source 3FGL J1051.0+5332 with 68% (yellow) and 95% (green) confidence ellipses is shown. Squares mark the LDR1 sources which lie within the 95% confidence band; the three red diamonds are the sources which we assess to be the most likely match.

experience the resulting matches seem plausible, but we will be able to better quantify the success of this method as the LoTSS footprint increases. We will also be able to test the reliability of this method against other supervised (e.g. principal component analysis, as used by D'Abrusco et al. 2013) and unsupervised (e.g. k -means clustering) machine learning techniques. However, these algorithms can only successfully identify quintessential blazars and those for which *WISE* data are available. For the UGS in this study without a likely match, it is possible that the counterparts lie beyond the blazar strip, where the synchrotron radiation is not the dominant component at IR wavelengths.

5. Conclusions

We examined the radio properties of the high-energy sources from BZCAT and 3FGL within LDR1. Because of their broadband nature, studying how blazars behave at low frequencies is essential to understanding how they operate. Historically, studying the low-frequency properties of blazars as a population has proven difficult because it has not been possible to identify low-frequency radio counterparts to these high-energy sources with the limited angular resolution and sensitivity of ~ 100 MHz surveys. The LDR1 catalogue addresses this technological gap and it is a marked improvement over even recent low-frequency surveys, such as MWACS and TGSS ADR1, in terms of angular resolution and sensitivity. As a result, we were able to find counterparts for all 3FGL and BZCAT sources in our field (excluding the UGS).

Despite their poorly-constrained γ -ray position and the density of sources in the LDR1 field, we were able to identify possible radio counterparts for two of the four UGS within the LDR1 footprint using the *WISE* colour information provided in the value-added catalogue. The radio spectral index was not available for most of the possible counterparts as the sources only had an LDR1 detection in the radio regime, but the availability of LoTSS in-band spectral indices in a future data release could help in matching these UGS.

The 100% detection rate of blazars in this study, alongside the wealth of ancillary information in the value-added catalogue makes the LoTSS first data release an extremely useful resource in studying the low-frequency properties of these high-energy sources. Indeed, preliminary efforts suggest that it may be possible to use LDR1 to discover new blazars in the field, for follow up with other instruments. We looked to use this k -NN method to identify sources in LDR1 which are possibly blazars. From the 218 595 sources with four *WISE* colours, $\sim 1\%$ fell within the blazar-populated space for all of the colour diagrams. This number could be cut down further by placing sensible limitations on the redshift and spectral index and this will be investigated in a future study.

In total, there are 1 444 3FGL sources and 2 138 BZCAT sources in the northern hemisphere sky, which is the final goal

Table 5: Likely matches to the UGS are given. Only one source was detected in another survey (NVSS) which we used to calculate α . There is no uncertainty listed as the fit is degenerate. We also list whether or not the LDR1 sources can be found in the Million Quasar Catalogue (MQC) (Flesch 2017), which is a compendium of quasars and high-confidence quasar candidates.

3FGL name	LDR1 name	Separation ($^{\circ}$)	MQC	z	α	S_{MHz} (mJy)
3FGL J1051.0+5332	ILTJ104931.19+533623.6	0.235	Yes	1.2582	–	1.17 ± 0.14
3FGL J1051.0+5332	ILTJ105106.97+533143.0	0.023	Yes	1.1291	–	0.85 ± 0.19
3FGL J1051.0+5332	ILTJ105238.00+533738.3	0.247	Yes	0.4025	-0.34	15.23 ± 0.25
3FGL J1103.3+5239	ILTJ110327.25+523425.1	0.09	No	0.3716	–	1.06 ± 0.11

of LoTSS in terms of sky coverage. As LoTSS progresses, we plan to revisit this work and evaluate the properties of blazar subclasses. The inherent variability of blazars will be an ever-present issue because the different observational methods for the radio and γ -ray regimes means that acquiring perfectly contemporaneous observations is challenging. But a larger sample size means we will be able to deduce general trends with more confidence and this should reduce the influence of flaring blazars. It is fortunate that LoTSS comes at a time when *Fermi* is still operational because *Fermi* is unrivaled with respect to γ -ray detections. Weaker γ -ray sources will be present in 4FGL, the next *Fermi*-LAT catalogue which is due to be released in 2018. The radio counterparts of these sources will be fainter too, possibly with more high-frequency-peaked BL Lacs, and LoTSS will be a valuable resource when it comes to identifying these sources.

Acknowledgements. SM acknowledges support from the Irish Research Council Postgraduate Scholarship and the Irish Research Council New Foundations Award. RM gratefully acknowledges support from the European Research Council under the European Union’s Seventh Framework Programme (FP/2007-2013)/ERC Advanced Grant RADIOLIFE-320745. HR and KJD acknowledge support from the ERC Advanced Investigator programme NewClusters 321271. LKM acknowledges support from Oxford Hintze Centre for Astrophysical Surveys, which is funded through generous support from the Hintze Family Charitable Foundation. This publication arises from research partly funded by the John Fell Oxford University Press (OUP) Research Fund. PNB is grateful for support from the UK STFC via grant ST/M001229/1. GG acknowledges the CSIRO OCE Postdoctoral Fellowship. MJH acknowledges support from the UK Science and Technology Facilities Council [ST/M001008/1]. IP acknowledges support from INAF under PRIN SKA/CTA ‘FORECaST’. JS is grateful for support from the UK STFC via grant ST/M001229/1. WLW acknowledges support from the UK Science and Technology Facilities Council [ST/M001008/1]. This paper is based (in part) on data obtained with the International LOFAR Telescope (ILT) under project code s LC2_038 and LC3_008. LOFAR (van Haarlem et al. 2013) is the LOw Frequency ARray designed and constructed by ASTRON. It has observing, data processing, and data storage facilities in several countries, which are owned by various parties (each with their own funding sources), and are collectively operated by the ILT foundation under a joint scientific policy. The ILT resources have benefited from the following recent major funding sources: CNRS-INSU, Observatoire de Paris and Université d’Orléans, France; BMBF, MIWF-NRW, MPG, Germany; Science Foundation Ireland (SFI), Department of Business, Enterprise and Innovation (DBEI), Ireland; NWO, The Netherlands; The Science and Technology Facilities Council, UK; Ministry of Science and Higher Education, Poland. Part of this work was carried out on the Dutch national e-infrastructure with the support of the SURF Cooperative through grant e-infra 160022 & 160152. The LOFAR software and dedicated reduction packages on https://github.com/apmchev/GGRID_LRT were deployed on the e-infrastructure by the LOFAR e-infragroup, consisting of J. B. R. Oonk (ASTRON & Leiden Observatory), A. P. Mechev (Leiden Observatory) and T. Shimwell (ASTRON) with support from N. Danezi (SURFsara) and C. Schrijvers (SURFsara). This research has made use of data analysed using the University of Hertfordshire high-performance computing facility (<http://uhhpc.herts.ac.uk/>) and the LOFAR-UK computing facility located at the University of Hertfordshire and supported by STFC [ST/P000096/1]. This research has made use of the NASA/IPAC Extragalactic Database (NED), which is operated by the Jet Propulsion Laboratory, California Institute of Technology, under contract with the National Aeronautics and Space Administration. This research has made use of SciPy software (Jones et al. 2001–) and Topcat (Taylor 2005).

References

- Acero, F., Ackermann, M., Ajello, M., et al. 2015, ApJS, 218, 23
 Ackermann, M., Ajello, M., Allafort, A., et al. 2011, ApJ, 741, 30
 Ackermann, M., Ajello, M., Atwood, W. B., et al. 2015, ApJ, 810, 14
 Beckmann, V. & Shrader, C. 2012, in Proceedings of “An INTEGRAL view of the high-energy sky (the first 10 years)” - 9th INTEGRAL Workshop and celebration of the 10th anniversary of the launch., 69
 Bell, M. E., Murphy, T., Hancock, P. J., et al. 2018, Monthly Notices of the Royal Astronomical Society, sty2801
 Böttcher, M. 2007, Astrophysics and Space Science, 309, 95
 Callingham, J. R., Ekers, R. D., Gaensler, B. M., et al. 2017, ApJ, 836, 174
 Callingham, J. R., Gaensler, B. M., Ekers, R. D., et al. 2015, ApJ, 809, 168
 Chiang, J. & Mukherjee, R. 1998, ApJ, 496, 752
 Condon, J. J., Cotton, W. D., Greisen, E. W., et al. 1998, AJ, 115, 1693
 D’Abrusco, R., Massaro, F., Ajello, M., et al. 2012, ApJ, 748, 68
 D’Abrusco, R., Massaro, F., Paggi, A., et al. 2013, ApJS, 206, 12
 de Gasperin, F., Intema, H. T., & Fraail, D. A. 2018, MNRAS, 474, 5008
 Duncan, K. J. et al. in press, A&A
 Fan, X.-L., Bai, J.-M., Liu, H.-T., Chen, L., & Liao, N.-H. 2012, Research in Astronomy and Astrophysics, 12, 1475
 Fanti, C., Fanti, R., Dallacasa, D., et al. 1995, A&A, 302, 317
 Flesch, E. W. 2017, VizieR Online Data Catalog, 7280
 Foreman-Mackey, D., Hogg, D. W., Lang, D., & Goodman, J. 2013, PASP, 125, 306
 Giroletti, M., Massaro, F., D’Abrusco, R., et al. 2016, A&A, 588, A141
 Hill, G. J., Gebhardt, K., Komatsu, E., et al. 2008, in Astronomical Society of the Pacific Conference Series, Vol. 399, Panoramic Views of Galaxy Formation and Evolution, ed. T. Kodama, T. Yamada, & K. Aoki, 115
 Hurley-Walker, N., Callingham, J. R., Hancock, P. J., et al. 2017, MNRAS, 464, 1146
 Hurley-Walker, N., Morgan, J., Wayth, R. B., et al. 2014, PASA, 31, e045
 Intema, H. T., Jagannathan, P., Mooley, K. P., & Frail, D. A. 2017, A&A, 598, A78
 Jones, E., Oliphant, T., Peterson, P., et al. 2001–, SciPy: Open source scientific tools for Python, [Online; accessed 27 June 2018]
 Kovalev, Y. Y., Aller, H. D., Aller, M. F., et al. 2009, ApJ, 696, L17
 Lane, W. M., Cotton, W. D., van Velzen, S., et al. 2014, MNRAS, 440, 327
 Linford, J. D., Taylor, G. B., & Schinzel, F. K. 2012, ApJ, 757, 25
 Lister, M. L. & Marscher, A. P. 1997, ApJ, 476, 572
 Marscher, A. P. & Gear, W. K. 1985, ApJ, 298, 114
 Massaro, E., Maselli, A., Leto, C., et al. 2015, Ap&SS, 357, 75
 Massaro, F., D’Abrusco, R., Ajello, M., Grindlay, J. E., & Smith, H. A. 2011, ApJ, 740, L48
 McGilchrist, M. M. & Riley, J. M. 1990, MNRAS, 246, 123
 Mücke, A., Pohl, M., Reich, P., et al. 1997, A&A, 320, 33
 Nelder, J. A. & Mead, R. 1965, The Computer Journal, 7, 308
 Nori, M., Giroletti, M., Massaro, F., et al. 2014, ApJS, 212, 3
 Padovani, P., Ghisellini, G., Fabian, A. C., & Celotti, A. 1993, MNRAS, 260, L21
 Pandey-Pommier, M., Sirothia, S., Chadwick, P., et al. 2016, in SF2A-2016: Proceedings of the Annual meeting of the French Society of Astronomy and Astrophysics, ed. C. Reylé, J. Richard, L. Cambrésy, M. Deleuil, E. Pécontal, L. Tresse, & I. Vauglin, 373–378
 Pavlidou, V., Richards, J. L., Max-Moerbeck, W., et al. 2012, ApJ, 751, 149
 Rengelink, R. B., Tang, Y., de Bruyn, A. G., et al. 1997, A&AS, 124, 259
 Richards, J. L., Max-Moerbeck, W., Pavlidou, V., et al. 2011, ApJS, 194, 29
 Salamon, M. H. & Stecker, F. W. 1994, ApJ, 430, L21
 Shimwell, T. W., Röttgering, H. J. A., Best, P. N., et al. 2017, A&A, 598, A104
 Shimwell, T. W. et al. in press, A&A
 Sikora, M., Begelman, M. C., & Rees, M. J. 1994, ApJ, 421, 153
 Stecker, F. W., Salamon, M. H., & Malkan, M. A. 1993, ApJ, 410, L71
 Stern, D., Assef, R. J., Benford, D. J., et al. 2012, ApJ, 753, 30
 Taylor, M. B. 2005, in Astronomical Society of the Pacific Conference Series, Vol. 347, Astronomical Data Analysis Software and Systems XIV, ed. P. Shopbell, M. Britton, & R. Ebert, 29

- Tinti, S., Dallacasa, D., de Zotti, G., Celotti, A., & Stanghellini, C. 2005, A&A, 432, 31
Turziani, S., Hardcastle, M., Miller-Jones, J., Broderick, J., & Markoff, S. 2015, in IAU Symposium, Vol. 313, Extragalactic Jets from Every Angle, ed. F. Massaro, C. C. Cheung, E. Lopez, & A. Siemiginowska, 95–96
Urry, C. M. 1998, Advances in Space Research, 21, 89
Urry, C. M. & Padovani, P. 1995, PASP, 107, 803
van Haarlem, M. P., Wise, M. W., Gunst, A. W., et al. 2013, A&A, 556, A2
Wakely, S. P. & Horan, D. 2008, International Cosmic Ray Conference, 3, 1341
Williams, W. L. et al. submitted, A&A

Table 6: Sources in our sample listed alongside some key parameters. An electronic version of this table is available at <https://gitub.com/mooneyse/LDR1-blazars>.

Number	RA ($^{\circ}$)	Dec. ($^{\circ}$)	LDR1	BZCAT	3FGL	Classification	z	$S_{144\text{MHz}}$ (mJy)	α	$S_{\gamma}(0.1\text{-}100 \text{ GeV})$ ($10^{12} \text{ ph cm}^{-2} \text{ s MeV}$)	Γ
1	161.600121	53.907374	ILTJ104624.03+535426.5	SBZQJ1046+5354	—	FSRQ	1.712	130 \pm 26	-0.03 \pm 0.17	—	—
2	161.940807	54.627993	ILTJ104745.79+543740.7	SBZBJ1047+5437	—	BL Lac Candidate	0.622	4 \pm 1	0.21 \pm 0.2	—	—
3	162.816848	46.738246	ILTJ105116.04+464417.6	SBZUJ1051+4644	—	Uncertain	1.419	718 \pm 152	-0.41 \pm 0.13	—	—
4	163.488478	54.031036	ILTJ105357.23+540151.7	SBZQJ1053+5401	3FGL J1058.6+5627	Galaxy-dominated BL Lac	0.998	992 \pm 198	-0.61 \pm 0.13	(2.27 \pm 0.08) \times 10 ⁻¹²	1.945 \pm 0.025
5	164.556869	56.469764	ILTJ105837.65+562811.1	SBZBJ1058+4653	—	BL Lac	0.143	173 \pm 35	0.09 \pm 0.13	(1.52 \pm 0.16) \times 10 ⁻¹³	1.930 \pm 0.076
6	166.279471	46.888549	ILTJ10607.07+465318.7	SBZGJ1060+4653	—	Galaxy-dominated BL Lac	0.112	73 \pm 15	-0.19 \pm 0.2	—	—
7	166.76993	50.117706	ILTJ110704.78+501037.4	SBZBJ1107+5010	—	BL Lac	0.706	35 \pm 7	0.1 \pm 0.26	—	—
8	166.857565	52.325458	ILTJ110725.82+521931.6	SBZQJ1107+5219	—	FSRQ	0.945	47 \pm 9	0.64 \pm 0.21	—	—
9	167.773752	52.463669	ILTJ11105.70+522749.2	SBZQJ1111+5227	—	FSRQ	1.284	456 \pm 91	-0.63 \pm 0.12	—	—
10	169.488205	53.931894	ILTJ111757.17+535554.8	SBZBJ1117+5355	3FGL J1117.9+5355	BL Lac	2.953	16 \pm 3	-0.13 \pm 0.11	(1.52 \pm 0.16) \times 10 ⁻¹³	1.930 \pm 0.076
11	170.095916	54.074222	ILTJ112023.02+540427.2	SBZQJ1120+5404	—	FSRQ	0.923	1025 \pm 205	-0.61 \pm 0.12	—	—
12	171.056412	51.563419	ILTJ112413.54+513348.3	SBZGJ1124+5133	—	Galaxy-dominated BL Lac	0.235	87 \pm 17	-0.27 \pm 0.22	—	—
13	171.224277	49.56941	ILTJ112453.83+493409.8	SBZBJ1124+4934	3FGL J1124.9+4932	BL Lac	0.908	17 \pm 3	0.04 \pm 0.12	(1.68 \pm 0.34) \times 10 ⁻¹⁴	1.803 \pm 0.154
14	174.509231	48.981876	ILTJ113802.22+483854.7	3FGL J1138.2+4905	Uncertain	FSRQ	1.305	17 \pm 3	0.38 \pm 0.11	(3.98 \pm 0.71) \times 10 ⁻¹²	2.851 \pm 0.182
15	174.589363	47.755044	ILTJ113821.45+474518.1	SBZQJ1138+4745	—	FSRQ	0.77	968 \pm 194	-0.52 \pm 0.13	—	—
16	175.199387	46.366832	ILTJ114047.85+462200.6	SBZQJ1140+4622	—	FSRQ	0.115	182 \pm 36	-0.33 \pm 0.17	—	—
17	175.988012	51.041951	ILTJ114357.12+510231.0	SBZBJ1143+5102	—	BL Lac	—	91 \pm 18	-0.43 \pm 0.26	—	—
18	176.684008	53.945298	ILTJ114644.16+535643.0	SBZQJ1148+5356	—	FSRQ	2.209	411 \pm 82	0.02 \pm 0.15	—	—
19	177.235842	52.906973	ILTJ114856.60+525425.1	SBZQJ1150+5528	—	FSRQ	1.632	221 \pm 44	-0.38 \pm 0.13	—	—
20	177.500649	55.47248	ILTJ115000.16+552820.9	SBZGJ1150+5528	—	Galaxy-dominated BL Lac	0.138	156 \pm 31	0.01 \pm 0.15	—	—
21	178.139215	49.660091	ILTJ115233.41+493936.3	SBZQJ1152+4939	—	FSRQ	1.093	626 \pm 125	-0.8 \pm 0.14	—	—
22	178.351974	49.519345	ILTJ115324.47+493109.6	SBZQJ1153+4931	3FGL J1153.4+4932	FSRQ	0.334	6651 \pm 1331	-0.68 \pm 0.13	(1.45 \pm 0.05) \times 10 ⁻¹¹	2.379 \pm 0.030
23	179.611407	48.421098	ILTJ115826.74+482515.9	SBZQJ1158+4825	—	FSRQ	2.036	399 \pm 80	-0.21 \pm 0.17	—	—
24	180.191246	47.973316	ILTJ120045.90+475823.9	SBZGJ1200+4758	—	Galaxy-dominated BL Lac	0.27	290 \pm 58	-0.88 \pm 0.13	—	—
25	180.877599	48.052322	ILTJ120330.62+480308.3	SBZQJ1203+4803	—	FSRQ	0.343	77 \pm 15	-0.03 \pm 0.21	—	—
26	180.881573	54.502488	ILTJ120331.58+543008.9	SBZBJ1203+5430	—	BL Lac	0.478	172 \pm 34	-0.34 \pm 0.13	—	—
27	182.226107	54.699613	ILTJ120854.27+544158.6	SBZQJ1208+5441	3FGL J1208.7+5442	FSRQ	1.343	325 \pm 65	0.15 \pm 0.21	(2.01 \pm 0.07) \times 10 ⁻¹¹	2.543 \pm 0.035
28	183.253203	51.493158	ILTJ121300.77+512935.3	SBZBJ1213+5129	3FGL J1212.6+5135	BL Lac	0.796	112 \pm 22	-0.49 \pm 0.17	(1.38 \pm 0.29) \times 10 ⁻¹³	2.191 \pm 0.150
29	183.752901	50.037853	ILTJ121500.50+500216.2	SBZBJ1215+5002	—	BL Lac	1.545	57 \pm 11	0.22 \pm 0.15	(5.84 \pm 0.88) \times 10 ⁻¹⁴	1.919 \pm 0.111
30	183.79149	46.454279	ILTJ121509.96+462715.4	SBZQJ1215+4627	—	FSRQ	0.72	987 \pm 198	-0.57 \pm 0.12	—	—
31	184.402825	51.919516	ILTJ121736.68+51510.2	SBZQJ1217+5151	—	FSRQ	2.225	79 \pm 16	-0.01 \pm 0.18	—	—
32	184.776916	48.499021	ILTJ121906.46+482956.4	SBZQJ1219+4829	—	FSRQ	1.071	678 \pm 136	-0.02 \pm 0.16	—	—
33	185.282548	47.708018	ILTJ1221107.81+474228.8	SBZGJ1221+4742	—	Galaxy-dominated BL Lac	0.21	114 \pm 23	-0.5 \pm 0.19	—	—
34	185.912332	46.188986	ILTJ122338.96+461120.3	SBZQJ1223+4611	—	FSRQ	1.012	516 \pm 103	-0.22 \pm 0.16	—	—
35	185.970166	46.846568	ILTJ122352.84+465047.6	SBZGJ1223+4650	—	Galaxy-dominated BL Lac	0.261	12 \pm 2	0.03 \pm 0.2	—	—
36	186.04125	50.032069	ILTJ122409.90+500155.4	SBZQJ1224+5001	3FGL J1224.5+4957	FSRQ	1.065	48 \pm 10	-0.05 \pm 0.13	(6.08 \pm 1.01) \times 10 ⁻¹³	2.463 \pm 0.131
37	186.277633	48.576511	ILTJ122506.63+483435.4	SBZUJ1225+4834	—	Uncertain	0.647	393 \pm 79	-0.76 \pm 0.13	—	—
38	186.982246	49.549112	ILTJ122755.74+493256.8	SBZQJ1227+4932	—	FSRQ	0.551	256 \pm 51	-0.12 \pm 0.17	—	—
39	187.215764	48.967037	ILTJ122851.78+485801.3	SBZQJ1228+4858	3FGL J1228.7+4857	FSRQ	1.722	1194 \pm 239	-0.55 \pm 0.13	(2.53 \pm 0.41) \times 10 ⁻¹³	2.365 \pm 0.124
40	188.144944	48.359178	ILTJ123234.79+482133.0	SBZQJ1233+4821	—	Galaxy-dominated BL Lac	1.588	656 \pm 136	-0.38 \pm 0.13	—	—
41	188.454997	50.439943	ILTJ123349.20+502623.8	SBZGJ1233+5026	—	Galaxy-dominated BL Lac	0.207	997 \pm 199	-0.58 \pm 0.11	—	—
42	188.555614	47.897647	ILTJ123413.35+475351.5	SBZQJ1234+4753	—	FSRQ	0.374	255 \pm 51	0.13 \pm 0.15	—	—
43	188.878317	52.474719	ILTJ123530.80+522828.9	SBZQJ1235+5228	—	FSRQ	1.653	61 \pm 12	0.25 \pm 0.18	—	—
44	189.332619	53.431541	ILTJ123807.83+532553.5	SBZUJ1238+5325	—	Uncertain	0.347	578 \pm 116	-0.51 \pm 0.21	—	—
45	189.629331	54.114188	ILTJ123831.04+540651.0	SBZGJ1238+5406	—	Galaxy-dominated BL Lac	0.224	112 \pm 22	-0.4 \pm 0.15	—	—
46	189.784689	52.213247	ILTJ124308.33+521247.6	SBZGJ1243+5212	—	Galaxy-dominated BL Lac	0.2	148 \pm 30	-0.24 \pm 0.29	—	—
47	192.142403	51.468464	ILTJ124834.18+512806.4	SBZBJ1248+5128	3FGL J1248.0+5130	BL Lac	0.351	282 \pm 56	-0.41 \pm 0.12	(7.92 \pm 1.75) \times 10 ⁻¹⁴	2.163 \pm 0.170
48	193.30064	53.020266	ILTJ125312.15+530112.9	SBZBJ1253+5301	3FGL J1253.2+5300	BL Lac	0.178	1172 \pm 235	-0.45 \pm 0.14	(2.74 \pm 0.12) \times 10 ⁻¹²	1.995 \pm 0.046
49	194.161109	53.573331	ILTJ125638.67+533423.9	—	3FGL J1256.7+5328	Uncertain	0.591	530 \pm 106	-0.48 \pm 0.13	(1.43 \pm 0.25) \times 10 ⁻¹²	2.639 \pm 0.125

Table 6 continued

Number	RA ($^{\circ}$)	Dec. ($^{\circ}$)	LDR1	BZCAT	3FGL	Classification	z	$S_{144\text{MHz}}$ (mJy)	α	$S_{\gamma(0.1-100\text{ GeV})}$ ($10^{-12}\text{ ph cm}^{-2}\text{ s MeV}^{-1}$)	Γ	
50	194.604893	51.706896	ILTJ125825.17+514224.8	—	3FGL J1258.7+51.37	Uncertain	0.441	217 \pm 43	-0.39 \pm 0.26	(5.19 \pm 1.25) \times 10 $^{-14}$	2.159 \pm 0.189	
51	195.135991	53.853585	ILTJ130032.64+535112.9	5BZBJ1300+5351	BL Lac	0.644	95 \pm 19	-0.47 \pm 0.16	—	—	—	
52	195.171868	50.493486	ILTJ130041.25+502936.5	5BZQJ1300+5029	FSRQ	1.564	839 \pm 168	-0.33 \pm 0.13	—	—	—	
53	195.571269	48.321771	ILTJ130217.10+481918.3	5BZQJ1302+4819	FSRQ	0.874	171 \pm 34	-0.09 \pm 0.22	—	—	—	
54	195.730643	50.938323	ILTJ130255.35+505617.9	5BZBJ1302+5056	BL Lac	0.686	3 \pm 1	-0.07 \pm 0.2	—	—	—	
55	196.513726	55.495609	ILTJ130603.29+552944.1	5BZQJ1306+5529	FSRQ	1.6	142 \pm 28	-0.07 \pm 0.13	—	—	—	
56	196.624684	47.692345	ILTJ130629.92+474132.4	5BZQJ1306+4741	FSRQ	2.543	52 \pm 10	-0.01 \pm 0.15	—	—	—	
57	197.213143	47.498457	ILTJ130851.15+472954.4	5BZQJ1308+4729	FSRQ	0.884	332 \pm 66	-0.65 \pm 0.13	—	—	—	
58	197.289151	55.959588	ILTJ130909.40+555734.5	5BZQJ1309+5557	FSRQ	1.631	292 \pm 58	-0.03 \pm 0.21	—	—	—	
59	197.722941	46.897592	ILTJ131053.51+465351.3	5BZQJ1310+4653	FSRQ	1.043	74 \pm 15	0.23 \pm 0.11	—	—	—	
60	197.762372	55.231595	ILTJ131102.97+551353.7	5BZQJ1311+5513	3FGL J1310.7+5515	FSRQ	0.926	587 \pm 118	-0.18 \pm 0.17	(9.09 \pm 1.55) \times 10 $^{-13}$	2.527 \pm 0.138	
61	198.043184	48.1564	ILTJ131210.36+480923.0	5BZQJ1312+4809	—	FSRQ	0.715	552 \pm 10	-0.49 \pm 0.17	—	—	—
62	198.180562	48.475364	ILTJ131243.33+482831.3	5BZUJ1312+4828	3FGL J1312.7+4828	Uncertain	0.489	474 \pm 95	-0.28 \pm 0.15	(2.59 \pm 0.07) \times 10 $^{-11}$	2.131 \pm 0.032	
63	199.876209	48.850909	ILTJ131930.29+485103.2	5BZQJ1319+4851	FSRQ	1.168	1 \pm 0	1.21 \pm 0.2	—	—	—	
64	201.122258	47.722542	ILTJ132429.34+474321.1	5BZQJ1324+4743	FSRQ	2.26	227 \pm 45	-0.09 \pm 0.14	—	—	—	
65	201.854737	50.146967	ILTJ132725.14+500849.0	5BZQJ1327+5008	FSRQ	1.025	786 \pm 157	-0.43 \pm 0.12	—	—	—	
66	202.520648	54.247706	ILTJ133004.96+541451.7	5BZQJ1330+5414	FSRQ	0.839	362 \pm 74	-0.65 \pm 0.14	—	—	—	
67	202.677516	52.037599	ILTJ13042.60+520215.3	5BZUJ1304+5202	3FGL J1330.9+5201	Uncertain	0.783	8 \pm 2	1.03 \pm 0.2	(7.24 \pm 1.51) \times 10 $^{-14}$	2.249 \pm 0.202	
68	203.188697	47.372615	ILTJ132949.29+472221.4	5BZQJ1330+5202	FSRQ	0.669	213 \pm 43	0.09 \pm 0.2	(2.05 \pm 0.26) \times 10 $^{-12}$	2.529 \pm 0.104		
69	203.474375	50.959978	ILTJ133042.60+520215.3	5BZUJ1330+5202	3FGL J1331.8+4718	FSRQ	1.362	68 \pm 14	-0.16 \pm 0.15	(2.34 \pm 0.20) \times 10 $^{-12}$	2.496 \pm 0.071	
70	203.654959	56.529912	ILTJ133347.19+563147.6	5BZQJ1334+5631	FSRQ	0.343	714 \pm 143	-0.62 \pm 0.12	—	—	—	
71	204.456888	55.017399	ILTJ133749.65+550102.6	5BZQJ1337+5501	FSRQ	1.099	586 \pm 117	0.03 \pm 0.13	—	—	—	
72	205.400755	55.243832	ILTJ134136.18+551437.8	5BZBJ1341+5514	3FGL J1341.5+5517	BL Lac	0.207	54 \pm 11	-0.1 \pm 0.17	(6.12 \pm 1.12) \times 10 $^{-13}$	2.563 \pm 0.169	
73	206.439252	53.548524	ILTJ134545.42+533254.6	5BZUJ1345+5332	Uncertain	0.136	1334 \pm 267	-0.5 \pm 0.15	—	—	—	
74	207.394163	53.688067	ILTJ134934.60+534117.0	5BZQJ1349+5341	FSRQ	0.979	2233 \pm 447	-0.31 \pm 0.14	—	—	—	
75	207.992576	55.702997	ILTJ135158.22+554210.7	5BZBJ1351+5542	BL Lac	0.224	35 \pm 7	0.52 \pm 0.22	—	—	—	
76	208.366892	56.015809	ILTJ135228.05+560056.9	5BZBJ1353+5600	BL Lac	0.404	17 \pm 3	-0.04 \pm 0.17	—	—	—	
77	209.773803	55.741439	ILTJ135905.71+554429.1	5BZQJ1359+5544	FSRQ	1.013	96 \pm 19	0.46 \pm 0.41	(5.39 \pm 0.42) \times 10 $^{-12}$	2.593 \pm 0.068		
78	213.903322	48.508372	ILTJ141536.80+483030.1	5BZBJ1415+4830	BL Lac	0.496	21 \pm 4	0.24 \pm 0.3	(1.89 \pm 0.29) \times 10 $^{-12}$	2.669 \pm 0.155		
79	214.281187	46.11776	ILTJ141707.48+460703.9	5BZQJ1417+4607	—	FSRQ	1.554	2988 \pm 598	-0.5 \pm 0.13	—	—	
80	214.939704	54.387341	ILTJ141945.53+542314.4	5BZBJ1419+5423	3FGL J1419.9+5425	BL Lac	0.152	640 \pm 128	0.09 \pm 0.17	(1.62 \pm 0.11) \times 10 $^{-12}$	2.308 \pm 0.062	
81	215.086649	46.412448	ILTJ142020.80+462444.8	5BZQJ1420+4624	FSRQ	1.244	6 \pm 1	0.87 \pm 0.2	—	—	—	
82	215.346061	46.763346	ILTJ142123.05+464548.0	5BZQJ1421+4645	FSRQ	1.669	38 \pm 8	0.52 \pm 0.2	—	—	—	
83	215.775784	48.036404	ILTJ142306.19+480211.0	5BZQJ1423+4802	—	FSRQ	2.232	397 \pm 79	-0.02 \pm 0.13	—	—	
84	216.873141	54.155871	ILTJ142729.55+540921.1	5BZQJ1427+5409	Galaxy-dominated BL Lac	0.106	128 \pm 26	-0.46 \pm 0.14	—	—	—	
85	217.341103	54.103115	ILTJ142921.86+540611.2	5BZQJ1429+5406	FSRQ	3.03	3550 \pm 710	-0.58 \pm 0.13	—	—	—	
86	219.239702	56.656725	ILTJ143657.53+563924.2	5BZBJ1436+5639	BL Lac	0.756	52 \pm 10	-0.39 \pm 0.17	(7.00 \pm 0.96) \times 10 $^{-14}$	1.985 \pm 0.127		
87	219.319563	47.29049	ILTJ143716.70+471725.7	5BZQJ1437+4717	BL Lac	0.944	468 \pm 94	-0.74 \pm 0.13	—	—	—	
88	219.942255	46.053169	ILTJ143946.14+460311.4	5BZQJ1439+4603	BL Lac	1.023	185 \pm 37	-0.12 \pm 0.12	—	—	—	
89	219.946582	49.968528	ILTJ144747.18+495806.7	5BZQJ1447+4958	BL Lac	0.174	218 \pm 46	-0.27 \pm 0.15	(3.45 \pm 0.37) \times 10 $^{-12}$	2.602 \pm 0.105		
90	220.756555	52.027279	ILTJ144301.53+520138.2	3FGL J1442.6+5156	Radio galaxy	0.141	14098 \pm 2821	-0.78 \pm 0.12	(1.83 \pm 0.51) \times 10 $^{-14}$	1.912 \pm 0.184		
91	222.750341	52.019887	ILTJ145100.08+520111.5	5BZQJ1450+5201	BL Lac	2.471	69 \pm 14	0.31 \pm 0.34	(2.41 \pm 0.33) \times 10 $^{-13}$	2.177 \pm 0.094		
92	223.614342	51.409562	ILTJ145427.44+512434.4	5BZQJ1454+5124	BL Lac	1.083	654 \pm 131	-0.58 \pm 0.13	(1.59 \pm 0.08) \times 10 $^{-12}$	2.084 \pm 0.036		
93	224.015284	50.807276	ILTJ145603.67+504826.2	5BZQJ1456+5048	BL Lac	1.379	30 \pm 6	—	—	—	—	
94	224.614145	48.546108	ILTJ145827.39+483245.9	5BZQJ1458+4832	BL Lac	0.541	3 \pm 1	0 \pm 0.2	—	—	—	
95	225.203022	47.853805	ILTJ150048.73+475113.7	5BZQJ1500.6+4750	FSRQ	1.059	565 \pm 113	-0.18 \pm 0.14	(7.07 \pm 1.48) \times 10 $^{-13}$	2.643 \pm 0.149		
96	225.275763	55.464006	ILTJ150101.06+552750.4	5BZQJ1501+5527	BL Lac	—	9 \pm 2	0.08 \pm 0.2	—	—	—	
97	225.950377	47.992007	ILTJ150348.09+475931.2	5BZQJ1503+4759	BL Lac	0.159	69 \pm 14	0.06 \pm 0.17	(1.26 \pm 0.19) \times 10 $^{-13}$	2.218 \pm 0.134		
98	226.683827	49.565557	ILTJ150644.12+493356.0	5BZQJ1506+4933	FSRQ	1.544	91 \pm 20	-0.04 \pm 0.18	—	—	—	